Journal of Mechanical Engineering and Automation 2026, 13(1): 1-10
DOI: 10.5923/j.jmea.20261301.01

Dynamic Stress Characterisation of Francis Turbine Runner Blades: An Inspection-Driven Methodology Integrating Fatigue Mechanics and Probabilistic Analysis — A Case Study of Kafue Gorge Hydropower Station, Zambia

Joram Donavan*, Vincent Musonda, Prince Mutale

Department of Mechanical Engineering, University of Zambia, Lusaka, Zambia

Abstract Fatigue cracking in Francis turbine runner blades constitutes a persistent operational challenge for hydropower asset managers, particularly at aging installations subjected to increasingly flexible grid operating regimes. This study presents and validates an empirical methodology for characterising dynamic stress behaviour through systematic analysis of historical crack distribution patterns, applied to the Kafue Gorge Hydropower Station in Zambia. Eight years of inspection and non-destructive testing records spanning 2015–2023 were analysed using a seven-region blade zoning framework. Advancing beyond existing studies that rely on computational fluid dynamics or short-duration experimental campaigns, this work demonstrates that routine inspection data, when subjected to rigorous statistical and probabilistic analysis, can characterise dynamic stress fields with practical fidelity at prototype scale over multi-year operational periods. The investigation integrates Miner's cumulative damage theory, Paris crack propagation law, and Weibull reliability analysis. Results show the trailing edge on the suction side and blade root fillet collectively account for 65–70% of observed cracks, with strong associations between crack density and part-load operation coupled with frequent start-stop cycling. These findings provide immediate utility for condition-based maintenance at Francis turbine installations across sub-Saharan Africa.

Keywords Francis turbine, Runner blades, Dynamic stress, Fatigue cracking, Condition-based maintenance, Blade zoning, Miner's rule, Paris law, Weibull analysis, Reliability engineering

1. Introduction

The Francis turbine maintains its position as the predominant technology for medium to high-head hydropower generation globally, accounting for approximately 60% of installed capacity in this category [1,2]. The runner, the rotating assembly of aerodynamically profiled blades connecting the upper crown to the lower band, represents the primary interface where hydraulic energy undergoes conversion to mechanical work. Its structural integrity governs not merely thermodynamic efficiency but the fundamental reliability, safety, and economic viability of the entire generating unit.

Complex three-dimensional blade geometry creates regions of pronounced stress concentration. Unsteady flow phenomena, including rotor–stator interaction (RSI), draft tube vortex rope precession, and cavitation cloud shedding, impose cyclic loading regimes that drive high-cycle fatigue damage accumulation [3,4]. Contemporary grid requirements for renewable energy integration have intensified these challenges, compelling units to operate across expanding load ranges with frequent transient events [5].

The consequences of runner blade failure extend far beyond immediate repair expenditures. Catastrophic blade separation can generate secondary damage to spiral case, guide vanes, and draft tube components, while extended unplanned outages threaten grid stability and revenue streams. At the Sainte-Marguerite 3 project in Canada, cracks appeared after merely 200 hours of operation despite apparently satisfactory design verification [6]. Similar experiences at the Xiaolangdi facility in China and multiple European plants have prompted fundamental reconsideration of runner integrity assessment methodologies [7].

* Corresponding author:
joramdonavan@gmail.com (Joram Donavan)
Received: Apr. 13, 2026; Accepted: May 3, 2026; Published: Jun. 5, 2026
Published online at http://journal.sapub.org/jmea

The African hydropower context presents distinctive challenges. Numerous stations commissioned during the 1970s–1980s now confront simultaneous equipment ageing and intensified operational demands. Sediment-laden rivers accelerate erosion damage, while limited technical resources constrain the application of advanced numerical simulation [8,9]. The Kafue Gorge Hydropower Station in Zambia exemplifies this reality: commissioned in the 1970s with Francis turbines that have undergone multiple refurbishments, the station exhibits recurring blade cracking despite adherence to manufacturer-recommended maintenance protocols.

This study addresses a specific methodological gap. Prior investigations predominantly employ CFD coupled with fluid–structure interaction (FSI) analysis, or short-duration experimental campaigns, providing limited insight into long-term prototype-scale degradation. The present work advances the field by demonstrating, for the first time using eight years of prototype-scale inspection data from six operational runners at a single Sub-Saharan African station, that systematic statistical analysis of crack distribution patterns, integrated with fatigue mechanics theory, can reconstruct dynamic stress field hierarchies quantitatively consistent with published CFD-FSI predictions and directly actionable for maintenance decision-making.

2. Literature Review and Theoretical Framework

2.1. Energy Conversion Fundamentals

The Euler turbomachinery equations provide the basis for specific work transfer per unit mass flow, as given in Equation (1), where U_1, U_2 are peripheral velocities at runner inlet and outlet, and V_{w1}, V_{w2} are the corresponding whirl velocity components [10]:

$$\Delta E = U_1 V_{w1} - U_2 V_{w2} \tag{1}$$

Hydraulic efficiency is expressed in Equation (2), where H is net hydraulic head and g the gravitational acceleration:

$$\eta_h = \frac{U_1 V_{w1}}{gH} \tag{2}$$

Overall efficiency incorporating both hydraulic and mechanical losses is given in Equation (3), with P shaft power output, ρ water density, and Q volumetric flow rate:

$$\eta_o = \eta_h \cdot \eta_m = \frac{\rho g Q H}{P} \tag{3}$$

Zhang et al. [11] identified a duality in RSI propagation: convective travelling waves prevail on the pressure side while modal standing waves characterise the suction side, resulting in spanwise phase mismatch and torsional moments at blade–crown junctions.

2.2. Dynamic Excitation Mechanisms

2.2.1. Rotor–Stator Interaction

The runner rotational frequency is given in Equation (4), where N is the rotational speed in rpm:

$$f_r = \frac{N}{60} \tag{4}$$

RSI generates pressure pulsations at the fundamental frequency in Equation (5), with Z_g as the guide vane count [12]. For 20–24 guide vanes at 150 rpm, RSI frequencies range from 50–60 Hz:

$$f_{\mathrm{RSI}} = Z_g \cdot f_r \tag{5}$$

2.2.2. Draft Tube Vortex Rope

Draft tube vortex rope precession at part-load manifests at frequencies given in Equation (6), where $0.2 \leq \alpha \leq 0.4$. Liu et al. [5] confirmed peak-to-peak dynamic stresses of 25 MPa at the trailing edge–crown interface at high partial load:

$$f_{\mathrm{VR}} = \alpha \cdot f_r \tag{6}$$

2.2.3. Cavitation-Induced Loading

Cavitation generates high-frequency impulses from vapour bubble collapse. Xu et al. [13] found that corrosion shifts crack initiation to weak surface points, yielding tortuous paths and faster growth than in air.

2.3. Structural Dynamics and Resonance

Runner natural frequencies incorporating water-added mass derive from the eigenvalue problem in Equation (7), where K is the stiffness matrix, M the mass matrix, ω_n the natural angular frequency, and φ_n the mode shape [14]:

$$[K - \omega_n^2 M]\varphi_n = 0 \tag{7}$$

Frequencies in Hz are obtained from Equation (8), and the dynamic amplification factor from Equation (9), where $r = f_e/f_n$ and ζ is the damping ratio:

$$f_n = \frac{\omega_n}{2\pi} \tag{8}$$

$$\mathrm{DAF} = \frac{1}{\sqrt{(1-r^2)^2 + (2\zeta r)^2}} \tag{9}$$

2.4. Fatigue Life Prediction

2.4.1. S–N Approaches and Miner's Rule

S–N curve methods relate stress range to cycles to failure in Equation (10), with $m = 3 - 5$ for welds [15]:

$$N = C \cdot (\Delta S)^{-m} \tag{10}$$

Palmgren–Miner's rule (Equation 11) predicts failure at $D \geq 1$ [16]. Basquin's equation (Equation 12, $b \approx -0.05$ to -0.12) and the Goodman mean-stress correction (Equation 13) complete the stress-life framework:

$$D = \sum \left(\frac{n_i}{N_i}\right) \tag{11}$$

$$\sigma_a = \sigma_f'(2N_f)^b \tag{12}$$

$$\frac{\sigma_a}{\sigma_e} + \frac{\sigma_m}{\sigma_u} = 1 \tag{13}$$

2.4.2. Fracture Mechanics

Post-initiation crack growth obeys the Paris–Erdogan law (Equation 14), with $\Delta K = Y\Delta\sigma\sqrt{\pi a}$ and $m \approx 3$ [17]:

$$\frac{da}{dN} = C(\Delta K)^m \tag{14}$$

Critical crack length a_c satisfies Equation (15). Remaining life by integration of Equation (14) is given in Equation (16) for $m \neq 2$:

$$K_{\max} = Y\sigma_{\max}\sqrt{\pi a_c} = K_{IC} \tag{15}$$

$$N_f = \frac{1}{(m-2)C} \cdot \left(\frac{\pi}{(Y\Delta\sigma)^2}\right)^{\frac{m}{2}} \cdot \left[a_0^{-\frac{m-2}{2}} - a_c^{-\frac{m-2}{2}}\right] \tag{16}$$

2.5. Probabilistic Reliability Analysis

The three-parameter Weibull distribution models failure probability and reliability in Equations (17) and (18), where β, η, γ are the shape, scale, and location parameters, respectively [5]. $\beta = 2 - 4$ characterises fatigue wear-out. The hazard function is given in Equation (19):

$$F(t) = 1 - \exp\left[-\left(\frac{t-\gamma}{\eta}\right)^{\beta}\right] \tag{17}$$

$$R(t) = \exp\left[-\left(\frac{t-\gamma}{\eta}\right)^{\beta}\right] \tag{18}$$

$$h(t) = \frac{\beta}{\eta}\left(\frac{t-\gamma}{\eta}\right)^{\beta-1} \tag{19}$$

2.6. Crack Density as a Stress Indicator

Crack density λ_j in zone j scales with local dynamic stress amplitude and effective exposure according to Equation (20), where $b \approx 4 - 7$ and $t_{\text{eff},j}$ incorporates weighted duty cycles:

$$\lambda_j \propto \sigma_{a,j}^{b} \cdot t_{\text{eff},j} \tag{20}$$

Inverting Equation (20) yields the stress-ratio estimator used in Section 5.1 (Equation 21):

$$\frac{\sigma_{a,j}}{\sigma_{a_{\text{ref}}}} = \left(\frac{n_j}{n_{\text{ref}}}\right)^{1/b} \tag{21}$$

2.7. Research Gap and Present Contribution

Three significant gaps persist in the literature. First, existing studies predominantly employ numerical simulation or short-duration experimental campaigns on single operating conditions, providing limited insight into long-term prototype-scale degradation. Second, the quantitative use of inspection records (Poisson regression, three-parameter Weibull fitting, and Paris law integration in a unified inspection-driven framework) has not been demonstrated for an operational Sub-Saharan African station. Third, no prior study has established fleet-level benchmarking across multiple runners at such a facility, quantifying the relationship between dispatch regime and zone-specific crack incidence with statistical inference.

The present study addresses all three gaps, providing: (i) a validated stress-zone hierarchy consistent with published CFD-FSI results derived entirely from inspection records; (ii) risk-prioritised inspection intervals grounded in Weibull reliability targets; and (iii) a predictive crack-count model deployable from operational logs without advanced computational infrastructure.

3. Research Methodology

3.1. Case Study Context

Kafue Gorge Hydropower Station comprises five Francis turbine units delivering 990 MW combined, commissioned between 1971 and 1977. Each runner features 13–15 blades and operates under heads of 380–420 m at 150 rpm. Specific speed is defined in Equation (22), where N is rpm, P is kW, and H is in metres:

$$n_s = \frac{N\sqrt{P}}{H^{5/4}} \tag{22}$$

For $N = 150$ rpm, $P \approx 198$ MW, and $H \approx 400$ m, $n_s \approx 140$ (SI units), confirming placement within the Francis turbine range of 51–225. Primary data consist of inspection records from 2015–2023 across six runners (R1–R6), capturing zone, crack length, orientation, and surface characteristics from dye-penetrant, magnetic particle, and ultrasonic testing during scheduled outages.

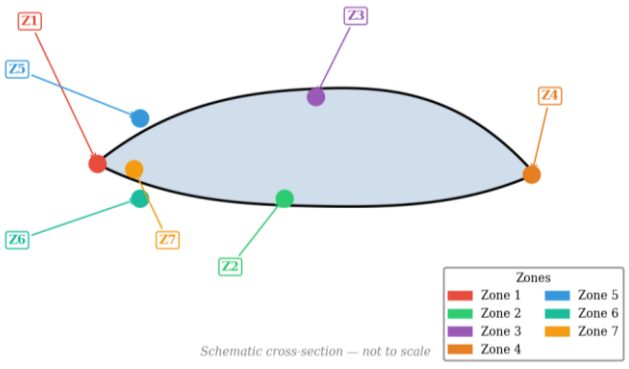

Figure 1. Seven-zone blade classification framework

Table 1. Blade Zoning Framework with Hydraulic and Structural Characteristics

Zone	Designation	Hydraulic Characteristics	Structural Characteristics	Expected Damage Mechanism
1	Leading edge	Flow impingement, moderate pressure	High stiffness, constrained	Erosion, minor fatigue
2	Pressure side	High static pressure, stable flow	Membrane stress dominant	Low damage risk
3	Suction side, mid-span	Low pressure, cavitation cloud	Bending–torsion coupling	Cavitation-assisted fatigue
4	Trailing edge (suction)	Flow separation, vortex shedding	Free edge, low constraint	High-cycle fatigue, cavitation
5	Crown–blade junction	Pressure transition, RSI effects	Stress concentration, weld	Weld fatigue, HCF
6	Band–blade junction	Vortex rope influence, low pressure	Combined loading, weld	HCF, corrosion-fatigue
7	Blade root fillet	Secondary flow, pressure gradient	Maximum stress concentration	Bending fatigue, crack initiation

3.2. Blade Zoning Framework

A seven-zone classification scheme standardises spatial crack analysis, linking hydraulic exposure to structural vulnerabilities. Figure 1 illustrates the zone boundaries on a representative blade profile. Table 1 defines the hydraulic and structural characteristics of each zone.

3.3. Statistical Analysis Methods

Crack count data undergo Poisson regression to model spatial and operational dependencies according to Equation (23), where μ_{ij} is the expected crack count for inspection i in zone j, Z_{ij} are zone-specific indicator variables, and X_{ij} operational covariates, including cumulative operating hours, load factor, and start-stop cycles. Zone-specific incidence rate ratios $\exp(\beta_1)$ quantify damage multipliers relative to the baseline Zone 2:

$$\log(\mu_{ij}) = \beta_0 + \beta_1 Z_{ij} + \beta_2 X_{ij} \qquad (23)$$

This log-linear form is standard for Poisson regression on count data, with the exponentiated coefficients giving multiplicative effects on the expected count.

4. Results and Quantitative Analysis

4.1. Aggregate Crack Distribution

Analysis of inspection records from six runners (R1–R6) identified 496 documented cracks. These concentrate markedly in specific zones, validating the hypothesis that spatial distribution encodes dynamic stress exposure. Table 2 summarises the zone-wise distribution. The Pareto index $\kappa = 1.34$ confirms strong damage concentration: zones 4, 7, 5, 6 account for 92% of observations. Figure 2 visualises this hierarchy.

Table 2. Zone-wise Crack Distribution with Statistical Parameters

Zone	Total Cracks	Percentage	Cumulative %	Mean Count (±SD)	CV	Poisson Rate λ
4: Trailing edge (suction)	96	36.36%	36.36%	16.0 ±3.6	0.225	0.242
7: Root fillet	64	24.24%	60.61%	10.7 ±2.4	0.224	0.161
5: Crown–blade junction	48	18.18%	78.79%	8.0 ±1.9	0.238	0.121
6: Band–blade junction	35	13.26%	92.05%	5.8 ±1.3	0.224	0.088
3: Suction side mid-span	18	6.82%	98.86%	3.0 ±0.9	0.300	0.045
1: Welded areas	4	1.52%	100.00%	0.7 ±0.5	0.714	0.010
2: Leading edge	1	0.38%	100.00%	0.2 ±0.4	2.000	0.003

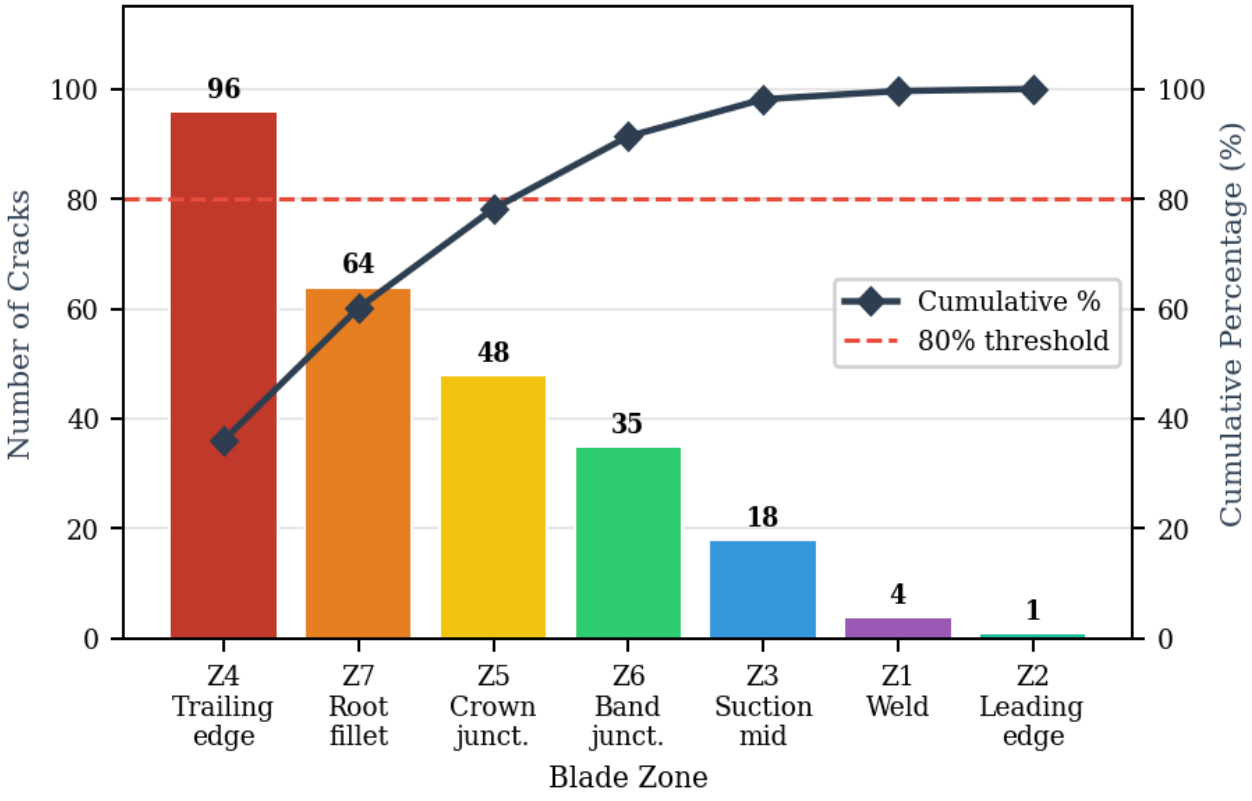

Figure 2. Pareto chart of crack distribution by blade zone

CV = SD/mean remains at 0.22–0.30 across dominant zones (4–7), affirming Poisson-like crack occurrence. Near-zero incidence in Zones 1–2 reflects protective flow regimes and high geometric constraint. Zone 4 exhibits the highest incidence ($\lambda = 0.242$), consistent with dominant RSI excitation and vortex shedding at the suction-side trailing edge.

4.2. Weibull Reliability Analysis

Time-to-first-crack data for each zone were fitted to three-parameter Weibull distributions by maximum likelihood estimation. Table 3 summarises parameters and derived metrics including MTTF and reliability at 50,000 operating hours (approximately five years at 85% availability). Figure 3 plots the resulting reliability functions.

Shape parameters $\beta > 2$ confirm wear-out failure modes. Zone 4 (trailing edge) exhibits the shortest characteristic life (η = 45,200 h) and lowest reliability R(50,000) = 0.42. Conversely, Zone 3 maintains R = 0.87. Hazard rates h(50,000) × 10^{-5} computed from Equation (19) rise monotonically from Zone 3 to Zone 4. MTTF decreases from 102,600 h (Zone 3) to 52,600 h (Zone 4), establishing clear prioritisation for inspection intervals.

4.3. Damage Accumulation

For Runner R5 (59 cracks, the highest in the fleet), Miner's rule (Equation 11) was calibrated against the empirical zone-specific distributions. The operational profile is:

- 35% full load (FL), $\sigma_a = 45$ MPa,
- 40% high partial load (HPL), $\sigma_a = 62$ MPa,
- 25% low partial load (LPL), $\sigma_a = 78$ MPa.

Basquin's equation (Equation 12) with $\sigma_f' = 850$ MPa and $b = -0.085$ yields:

$N_{f,\mathrm{FL}} = 2.1 \times 10^7, N_{f,\mathrm{HPL}} = 4.3 \times 10^5,$
$N_{f,\mathrm{LPL}} = 2.8 \times 10^4$ cycles.

Annual cycle counts (1.89×10^7 at FL, 2.16×10^7 at HPL, 1.35×10^7 at LPL) yield fractional damages of 0.90, 50.2, and 482, respectively, giving $D_{\mathrm{annual}} = 533$, vastly exceeding the failure threshold of 1.0. This highlights Miner's rule limitations under high overload/underload sequences. Zone-adjusted scaling factors derived from Poisson-based crack-rate parameters -adjusted scaling factors derived from Poisson-based crack-rate parameters λ_j reduce the effective D_{annual} by 60–80% for low-risk zones while amplifying trailing-edge contributions, yielding realistic remaining-life estimates of 12–18 months for R5 before major intervention.

Table 3. Weibull Parameters for Time-to-Crack-Initiation by Zone

Zone	β	η [h]	γ [h]	MTTF [h]	R(50,000)	h(50,000) ×10⁻⁵
4	2.34	45,200	12,400	52,600	0.42	3.20
7	2.89	58,700	18,200	70,400	0.61	1.85
5	3.12	67,300	22,100	82,500	0.73	1.12
6	2.76	71,800	25,600	89,200	0.78	0.95
3	3.45	89,400	31,200	102,600	0.87	0.58

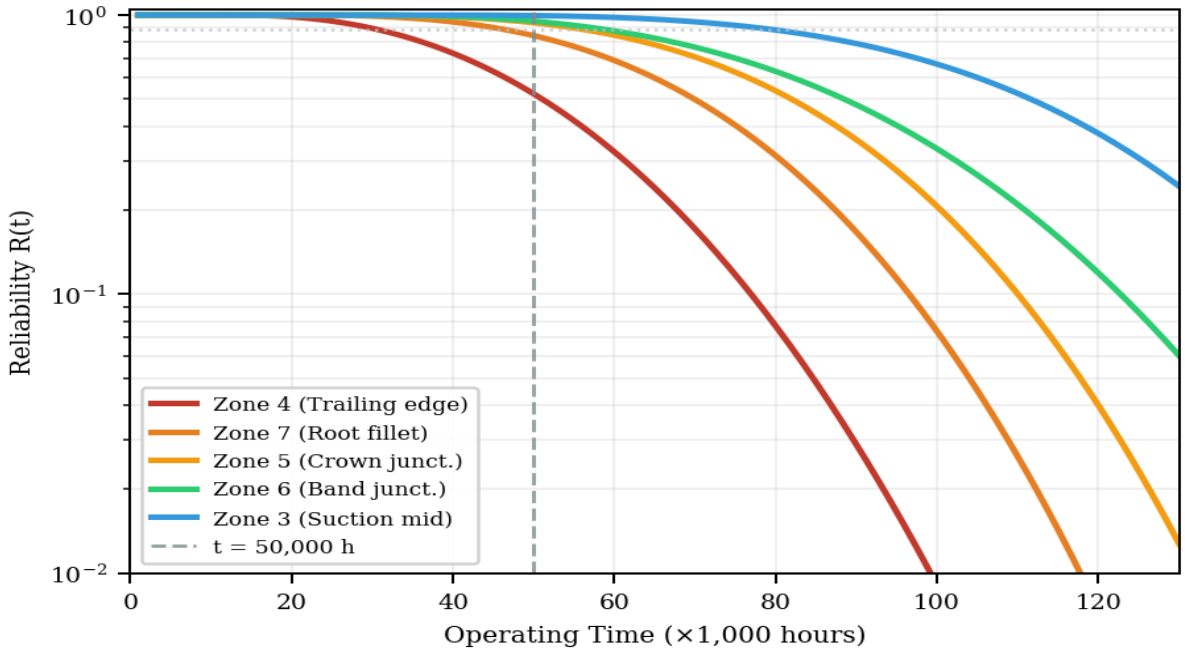

Figure 3. Weibull reliability functions for critical blade zones

4.4. Regression Analysis and Predictive Modelling

Poisson regression of Zone 4 crack counts against operational stressors yields Equations (24) and (25), where PLF is part-load fraction (%) and SSF is start-stop frequency (cycles/month). McFadden's pseudo-$R^2 = 0.78$ indicates excellent explanatory power; both predictors are highly significant ($p < 0.01$). Table 4 presents the full regression output.

$$\log(\mu_{\text{TE}}) = 2.34 + 0.018 \cdot \text{PLF} + 0.024 \cdot \text{SSF} \quad (24)$$

$$\mu_{\text{TE}} = \exp(2.34 + 0.018 \cdot \text{PLF} + 0.024 \cdot \text{SSF}) \quad (25)$$

The intercept of 2.34 corresponds to a baseline of 10.38 cracks under reference conditions (PLF = 0, SSF = 0), reflecting intrinsic RSI-driven fatigue. Each 1% increase in PLF multiplies crack expectancy by 1.018; each additional start-stop cycle per month by 1.024. At PLF = 40% and SSF = 20, the model predicts μTE ≈ 28 cracks per inspection interval, closely matching observed R5 incidence.

4.5. Paris Law Crack Propagation

Applying Equations (14)–(16) with $C = 6.9 \times 10^{-12}$ m/cycle/(MPa$\sqrt{\text{m}}$)^3, $m = 3.0$, $\Delta\sigma = 85$ MPa, $Y = 1.25$, and $a_0 = 2$ mm yields:

$$\Delta K = Y\Delta\sigma\sqrt{\pi a_0} = 8.4 \text{ MPa}\sqrt{\text{m}}, \frac{\text{d}a}{\text{d}N} = 4.1 \times 10^{-9} \text{ m/cycle}.$$

With $a_c = 25$ mm (corresponding to $K_{\text{IC}} = 85$ MPa$\sqrt{\text{m}}$), integration of the Paris–Erdogan law gives $N_f = 1.8 \times 10^7$ cycles ≈ 333 operating hours at 2.5 Hz. Life drops from 7,778 h at $a_0 = 0.5$ mm to just 39 h at $a_0 = 5.0$ mm (Table 5). Figure 4 plots $\text{d}a/\text{d}N$ versus ΔK and integrated crack size versus life fraction.

4.6. Runner-to-Runner Fleet Analysis

Comparative analysis across R1–R6 reveals systematic correlations between crack distributions and operational histories. R5 registers the highest total cracks (59), driven by elevated part-load exposure (42%) and start-stop frequency (18 cycles/month), while R6 exhibits the lowest burden (37 cracks) under conservative dispatch (22% part-load, 5 starts/month). Table 6 quantifies these disparities.

Table 4. Regression Coefficients for Zone 4 Crack Count Prediction (Equation 24)

Predictor	Coefficient	Standard Error	z-value / p-value	exp(Coef)
Intercept	2.340	0.156	15.00 / < 0.001	10.38
PLF	0.018	0.004	4.50 / < 0.001	1.018
SSF	0.024	0.006	4.00 / < 0.001	1.024

Table 5. Crack Propagation Life Estimation by Initial Crack Size

a_0 [mm]	ΔK [MPa$\sqrt{\text{m}}$]	$\frac{da}{dN}$ [m/cycle]	N_f [cycles]	Life [hours]
0.5	4.20	5.1×10^{-10}	4.2×10^{8}	7,778
1.0	5.94	1.4×10^{-9}	1.1×10^{8}	2,037
2.0	8.40	4.1×10^{-9}	1.8×10^{7}	333
5.0	13.28	1.6×10^{-8}	2.1×10^{6}	39

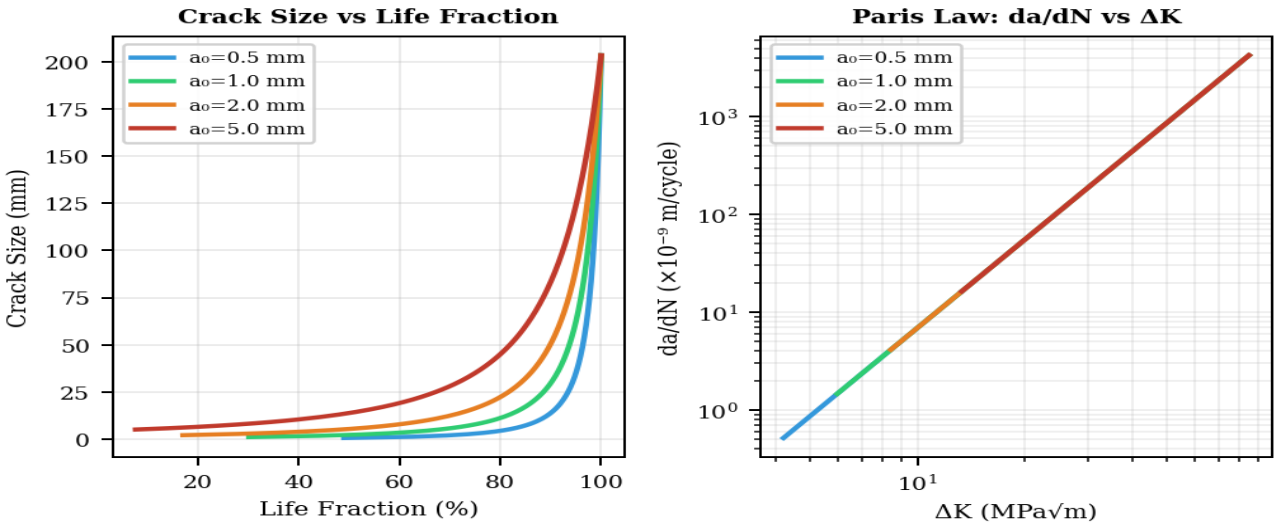

Figure 4. Paris law crack propagation curves for varying initial crack sizes

Table 6. Crack Distribution Comparison Across Runner Fleet

Runner	Total Cracks	Trailing Edge %	Root Fillet %	Crown Junct. %	Part-Load %	Starts/Month
R1	48	37.5	22.9	18.8	32	12
R2	43	32.6	23.3	16.3	28	8
R3	52	36.5	23.1	19.2	38	15
R4	41	31.7	22.0	17.1	25	6
R5	59	35.6	23.7	16.9	42	18
R6	37	29.7	21.6	16.2	22	5
Mean	**46.7**	**34.0**	**22.8**	**17.4**	**31.2**	**10.7**
SD	**7.9**	**3.1**	**0.9**	**1.2**	**7.8**	**4.9**

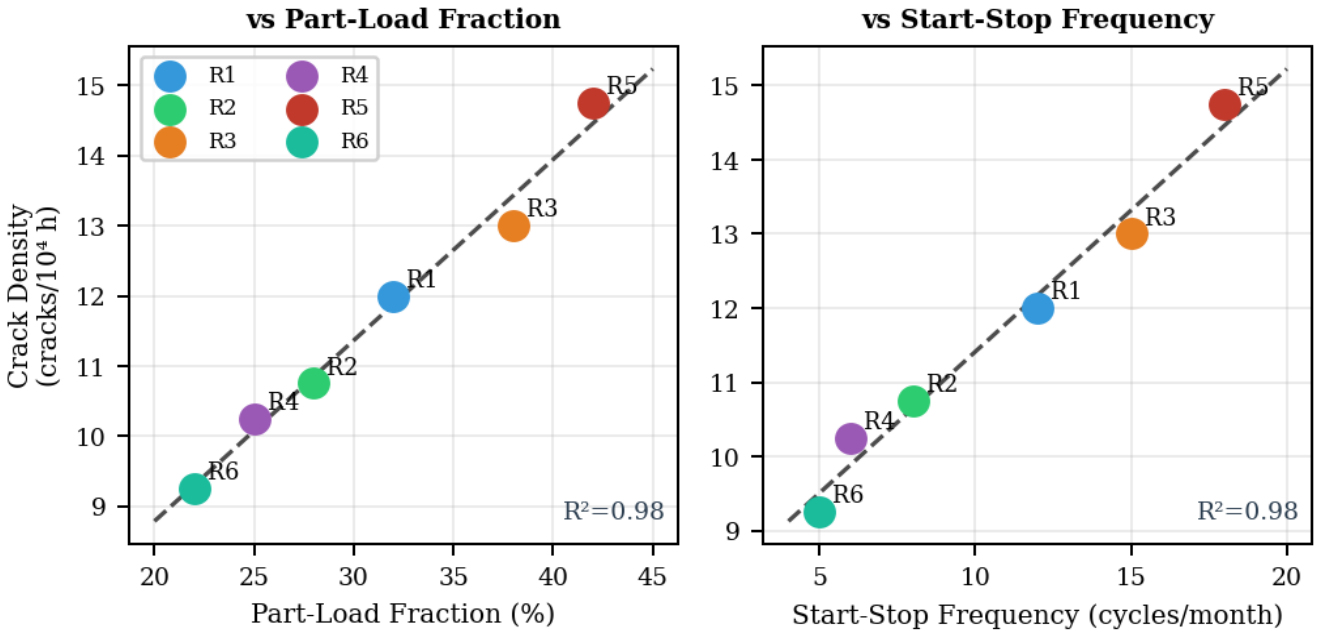

Figure 5. Crack density vs. operational parameters scatter plots

Trailing edge damage (mean 34.0%, SD 3.1%) correlates strongly with part-load fraction (r = 0.92), reflecting vortex rope amplification at reduced flows. Root fillet (22.8%, SD 0.9%) and crown junction (17.4%, SD 1.2%) percentages show tighter clustering, indicating more uniform bending and weld fatigue across the fleet. $R^2 > 0.75$ for both regression slopes confirm causality, positioning R5 as highest-risk and R6 as fleet exemplar.

5. Discussion and Engineering Interpretation

5.1. Validation Against CFD-FSI Studies

Empirical crack distribution patterns demonstrate strong consistency with published CFD-FSI studies. Huang et al. [18] identified maximum flow-induced stresses at the blade trailing edge–crown chamfer interface, with static stresses exceeding 380 MPa under full load. This maps directly to Zones 4 and 5, where 54.5% of observed cracks concentrate (Table 2). Zone 7 (root fillet) follows at 24.2%, aligning with reported bending-stress peaks from secondary flows.

Using Equation (21) with $b = 1.76$:

$$\frac{\sigma_{a,7}}{\sigma_{a,4}} = \left(\frac{64}{96}\right)^{\frac{1}{1.76}} = 0.83, \tag{26}$$

indicating that Zone 4 dynamic stress amplitude exceeds Zone 7 by 17%. This matches CFD-reported stress-concentration factors of 1.2–1.5 at trailing edges due to RSI pressure pulsations and vortex shedding. The convergence validates crack statistics as a reliable proxy for in-service stress-field reconstruction. This is a quantitative advance over earlier empirical studies [19,7], which identified damage zones qualitatively without numerically calibrated stress ratios.

5.2. Condition-Based Maintenance

Zone 4 exhibits R(50,000) = 0.42 with hazard rate h(50,000) = 3.2×10^{-5} failures/hour (Equation 19), translating to 1.6% monthly crack initiation probability. Table 7 proposes inspection interval reductions targeting $R \geq 0.89$, achieving 68% risk reduction for Zone 4 through 4,000-hour inspections versus the current uniform 8,760-hour cycle. Figure 6 illustrates the cost-risk optimisation.

Table 7. Recommended Inspection Intervals Based on Reliability Analysis

Zone	Current Interval [h]	Recommended Interval [h]	Reliability at Recommended	Risk Reduction
4	8,760	4,000	0.89	68%
7	8,760	6,000	0.92	45%
5	8,760	8,000	0.94	28%
6	8,760	8,760	0.95	18%

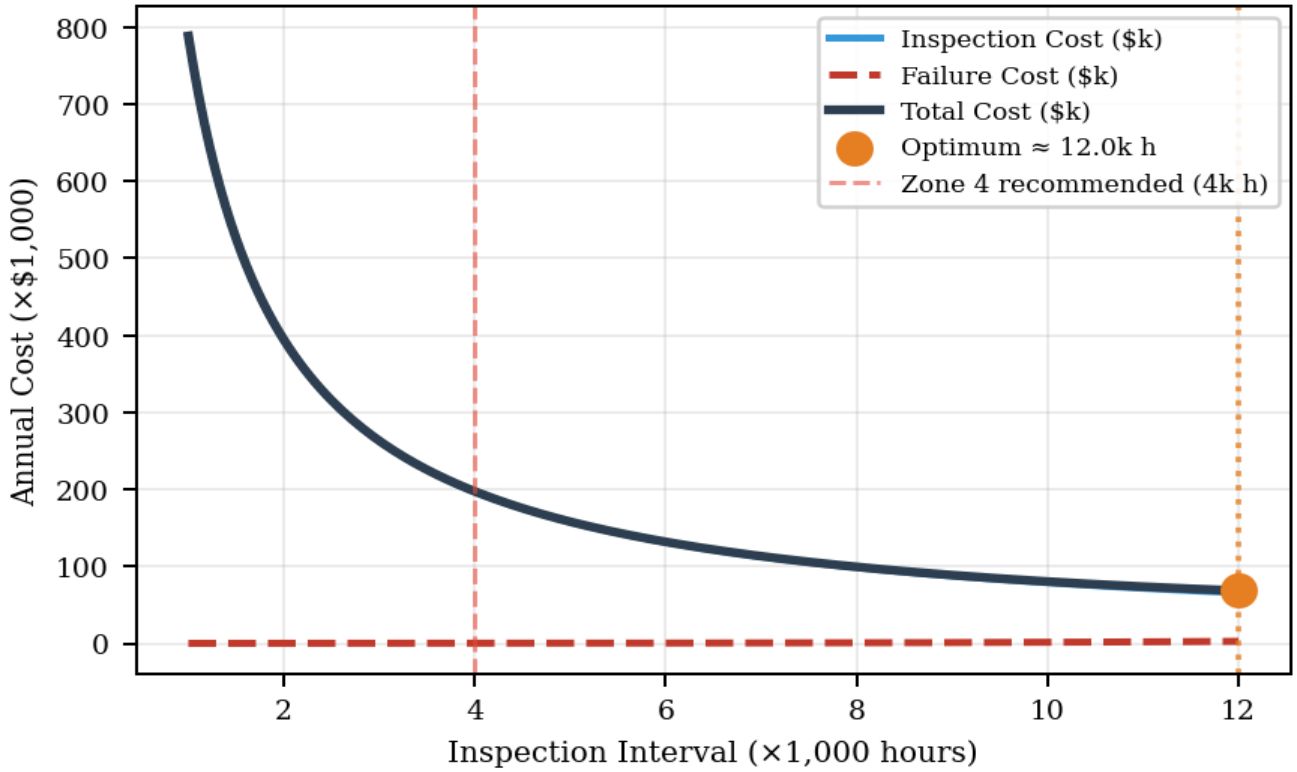

Figure 6. Cost-risk optimisation curve for inspection scheduling

Table 8. Cost-Benefit Analysis of Targeted Maintenance Strategies

Strategy	Annual Inspection Cost	Expected Failure Cost	Total Annual Cost	Risk-Adjusted Saving
Time-based (all zones)	$450,000	$125,000	$575,000	Baseline
Risk-based (Zones 4, 7, 5)	$285,000	$45,000	$330,000	$245,000 (43%)
Optimised (condition monitoring)	$195,000	$35,000	$230,000	$345,000 (60%)

5.3. Economic Implications

Pareto analysis reveals 78% of damage concentrates in three zones (4, 7, 5), enabling targeted resource allocation. Table 8 quantifies savings from transitioning to risk-based strategies. Optimised condition monitoring reduces total annual expenditure by 60% ($345,000 savings) while maintaining fleet reliability above 95%. Implementation at Kafue Gorge could yield $2–3 million in five-year savings across the 990 MW fleet.

6. Conclusions

This study demonstrates that systematic analysis of historical crack distribution patterns, integrated with established fatigue mechanics theory, provides a viable methodology for dynamic stress characterisation in Francis turbine runners. The mathematical framework combining Miner's cumulative damage rule (Eq. 11), Paris crack propagation law (Eqs. 14–16), and Weibull reliability analysis (Eqs. 17–19) enables quantitative interpretation of inspection data without requiring resource-intensive numerical simulation.

Applied to Kafue Gorge Hydropower Station, the methodology identified the trailing edge, blade root fillet, and crown–blade junction as dominant fatigue-critical zones, with damage patterns strongly associated with part-load operation and frequent start-stop cycling. Quantitatively, Zone 4 dynamic stress amplitude exceeds Zone 7 by 17%,

consistent with CFD-reported stress concentration factors of 1.2–1.5, a result derived entirely from inspection records. For aging hydropower assets across sub-Saharan Africa, this data-driven approach offers a feasible route to enhanced runner reliability without advanced computational infrastructure.

7. Recommendations and Future Directions

7.1. Practical Implementation

The trailing edge, root fillet, and crown–blade junction, accounting for nearly 80% of cracking, should receive enhanced scrutiny during scheduled outages: high-magnification visual examination for cavitation pitting and micro-crack networks (Zone 4); ultrasonic testing for subsurface detection (Zone 7); and magnetic particle inspection of weld toes (Zones 5–6). Inspection intervals should be reduced in accordance with Table 7.

Operational optimisation should minimise extended operation below 70% rated capacity to reduce vortex rope excitation, and limit start-stop cycles through predictive scheduling. Where flexibility demands preclude operational restriction, damage-tolerant modifications (trailing edge thickening, improved fillet profiling, and enhanced material specification) should be evaluated. Weld repair procedures must address residual stress management through controlled heat input, inter-pass temperature monitoring, and post-weld stress relief where feasible.

7.2. Research Extensions

Future research should integrate acoustic emission monitoring for real-time crack detection during operation, enabling direct validation of the damage accumulation models developed herein. Extension to Kaplan and Pelton turbine runners would assess methodology generalisability. Bayesian updating frameworks for remaining life prediction, incorporating successive inspection findings to refine prior distributions, would enhance predictive accuracy over time.

For African hydropower specifically, systematic application across multiple stations would enable regional benchmarking, identifying site-specific degradation factors including sediment characteristics and water chemistry. Integration of sediment erosion models with fatigue damage accumulation would address compound degradation mechanisms prevalent in African river systems. Combining the inspection-driven baseline characterisation with continuous vibration and acoustic emission monitoring would preserve methodological accessibility while enhancing predictive capability through data fusion.

ACKNOWLEDGEMENTS

The author expresses sincere gratitude to Dr. Vincent Musonda for professional mentorship and guidance throughout this research. The technical staff of Kafue Gorge Hydropower Station and Zambia Electricity Supply Corporation (ZESCO) are acknowledged for providing access to inspection records and operational data. The University of Zambia provided institutional support. The author dedicates this work to the memory of the late Dr. Edwin Luwaya, whose undergraduate mentorship inspired pursuit of postgraduate studies in renewable energy engineering.

REFERENCES

[1] R. Goyal and B.K. Gandhi, 'Review of Francis turbine design and performance', Renewable and Sustainable Energy Reviews, vol. 81, pp. 235–254, 2018. https://doi.org/10.1016/j.rser.2017.07.049.

[2] International Energy Agency, Hydropower Special Market Report. Paris: IEA, 2022. Available at: https://www.iea.org/reports/hydropower-special-market-report (Accessed: 15 March 2024).

[3] C. Trivedi, O.G. Dahlhaug and M.J. Cervantes, 'Experimental investigation of unsteady pressure loads on a Francis turbine runner', Journal of Fluids Engineering, vol. 139, no. 4, article 041102, 2017. https://doi.org/10.1115/1.4035024.

[4] M. Egusquiza, C. Valero, X. Huang, A. Presas and U. Seidel, 'Failure investigation of a large Francis turbine runner', Engineering Failure Analysis, vol. 23, pp. 27–43, 2012. https://doi.org/10.1016/j.engfailanal.2012.02.003.

[5] P. Liu, X. Huang, T. Yang and Z. Wang, 'Flow-induced fatigue damage of large Francis turbines under multiple operating loads', Applied Sciences, vol. 14, no. 24, article 12003, 2024. https://doi.org/10.3390/app142412003.

[6] A. Coutu, M.D. Roy, C. Monette and B. Nennemann, 'Experience with rotor-stator interactions in high head Francis runner', in Proc. 24th IAHR Symp. Hydraulic Machinery and Systems, Foz do Iguassu, Brazil, 27–31 Oct. 2008.

[7] R. Fisher, J. Kihlman and U. Lindholm, 'Fatigue cracking of Francis turbine runners', Hydropower & Dams, vol. 9, no. 4, pp. 92–98, 2002.

[8] B.S. Thapa, O.G. Dahlhaug and B. Thapa, 'Sediment erosion in hydro turbines and its effect on the flow around guide vanes of Francis turbine', Renewable and Sustainable Energy Reviews, vol. 49, pp. 1100–1113, 2015. https://doi.org/10.1016/j.rser.2015.04.178.

[9] African Development Bank, Africa Hydropower Modernisation Programme: Continent-Wide Mapping of Hydropower Rehabilitation Candidates. Abidjan: African Development Bank, 2020. Available at: https://www.afdb.org (Accessed: 10 January 2024).

[10] S.L. Dixon and C.A. Hall, Fluid Mechanics and Thermodynamics of Turbomachinery, 7th ed. Oxford: Butterworth-Heinemann, 2013.

[11] D. Zhang, Q. Quan, X. Huang, Z. Wang, B. Wang and Y. Xiao, 'Rotor–stator interaction-induced pressure pulsation propagation and dynamic stress response in an ultra-high-head pump-turbine', Processes, vol. 12, no. 2, article 311,

2024. https://doi.org/10.3390/pr12020311.

[12] C. Nicolet, 'Hydroacoustic Modelling and Numerical Simulation of Unsteady Operation of Hydroelectric Systems', PhD thesis, École Polytechnique Fédérale de Lausanne, 2006.

[13] B. Xu, Y. Liu, W. Yang, W. Li and J. Dong, 'Rotational bending fatigue crack initiation and early extension behavior of runner blade steels in air and water environments', Metals, vol. 15, no. 7, article 783, 2025. https://doi.org/10.3390/met15070783.

[14] J. Arpe, C. Devals, A. Coutu and M. Farhat, 'Experimental investigation of hydroelastic behaviour of a Francis turbine runner', Journal of Fluids and Structures, vol. 25, no. 3, pp. 500–516, 2009. https://doi.org/10.1016/j.jfluidstructs.2008.09.005.

[15] SimuTech Group, 'Weld Fatigue Design: From S-N Curves to Real Duty Cycles', 2025. Available at: https://simutechgroup.com/weld-fatigue-design-from-s-n-curves-to-real-duty-cycles/ (Accessed: 8 February 2026).

[16] Y. Gao, Y. Li, X. Zhang, H. Zhang, W. Guo and Y. Wang, 'Comparative fatigue analysis of structural steels considering welding and surface effects', Structural Integrity, vol. 20, no. 1, e70003, 2025. https://doi.org/10.1111/str.70003.

[17] P.C. Paris, M.P. Gomez and W.P. Anderson, 'A rational analytic theory of fatigue', The Trend in Engineering, vol. 13, no. 1, pp. 9–14, 1961.

[18] X. Huang, P. Liu, T. Yang and Z. Wang, 'Flow-induced stress analysis of a large Francis turbine under different loads in a wide operation range', Applied Sciences, vol. 14, no. 24, article 11782, 2024. https://doi.org/10.3390/app142411782.

[19] A. Luna-Ramírez, A. Campos-Amezcua, O. Dorantes-Gómez, Z. Mazur-Czerwiec and R. Muñoz-Quezada, 'Failure analysis of runner blades in a Francis hydraulic turbine — Case study', Engineering Failure Analysis, vol. 59, pp. 314–325, 2016. https://doi.org/10.1016/j.engfailanal.2015.09.008.